A Model-Based Series Arc Fault Detection Method for Multiterminal DC Microgrids

Ting Wang, *Member, IEEE*, Yanxin Chen, Wei Liu, Zhiguo Hao, *Senior Member, IEEE*, Antonello Monti, *Senior Member, IEEE*, and Ferdinanda Ponci, *Senior Member, IEEE*

***Abstract*—Timely and accurate detection of series arc faults in multiterminal dc microgrids is a challenging task. Existing series arc fault detection methods suffer from different deficiencies in terms of selectivity, applicability, and efficiency. To solve these problems, this article introduces a model-based series arc fault detection scheme for dc microgrids. First, a minimized system model dedicated to series arc fault detection is derived. On this basis, a bank of reduced-order unknown input observers are established. Through recognizing predefined patterns in the output of the observer bank, various series arc faults can be detected and isolated in a timely manner. The proposed method is advantageous in that it can simultaneously locate multiple series arc faults in complex dc microgrids without relying on auxiliary power hardware, special measurement devices, prior fault data, and avoid cumbersome threshold settings. The performance of the proposed method has been verified through numerical simulations with MATLAB/Simulink and experimental tests.**

***Index Terms*—DC microgrids, fault detection, protection, reduced-order unknown input observers, series arc faults.**

I. Introduction

RENEWABLE energy generating facilities, energy storage systems (ESSs) and electric vehicle chargers are booming in modern power systems. In the integration of these devices, which are essentially dc or embedded with dc links, dc microgrids offer multiple advantages in terms of controllability, flexibility, and efficiency [1].

However, series arc faults (SAFs) are still one of the major threats to the safety of dc microgrids. SAFs occur when plasma channels are formed in current-carrying wires due to wire breakage. DC SAFs are self-sustaining, which can lead to fire hazards in dc microgrids. Meanwhile, series arc currents are much lower than short-circuit fault currents, which can be undetectable with conventional protection devices.

So far, a number of series arc fault detection (SAFD) methods for dc microgrids have been proposed, which are reviewed in the following.

Signal-Based Methods: The time-domain variations in line currents and load voltages [2], [3], [4], and statistical features, such as the randomness [5], entropy [6], and derivation [7] in current signals, are used as the references for SAFD. Besides, the frequency-domain components of arc currents are extracted with fast Fourier transform [8], short-time Fourier transform [9], and wavelet transform [10] for SAFD. However, these methods lack selectivity in locating SAFs in multiterminal dc microgrids. Other SAFD methods rely on auxiliary power hardware, including shunt capacitors [11] and resonant filters [12], which restricts the applicability of these methods. Besides, SAFD is also achieved through detecting electromagnetic radiations [13], [14] emitted from dc SAFs. Yet these methods necessitate special sensors and antennas located in proximity to fault locations. These limitations in the existing signal processing-based methods are eliminated in the proposed method, as it solves the SAFD in multiterminal dc microgrids without using any additional power hardware or special sensors.

Data-Driven Methods: SAFD can be achieved with data-driven fault classification models. In [15], hidden Markov models using time–frequency and time-domain extracted features are introduced to discriminate between normal disturbances and SAFs in dc microgrids. In [16], ensemble learning models are trained to detect SAFs in dc microgrids. In [17], a multiclass AdaBoost algorithm is developed to classify multiple fault types, including SAFs, in dc microgrids. However, the training of these fault classification models requires abundant historical fault data, which can not be easily obtained in real-world dc microgrids. By comparison, the proposed method does not require any historical fault data.

Model-Based Methods: Model-based fault diagnosis methods make use of the analytical redundancy provided by mathematical models that characterize the dynamics of protected systems. Among different model-based methods, observers play a key role in fault diagnosis with deterministic models [18]. Existing research efforts on observer-based protection methods for dc microgrids have been mainly centered on converter switch

Received 13 December 2024; revised 2 April 2025 and 11 June 2025; accepted 26 July 2025. Date of publication 5 August 2025; date of current version 13 November 2025. This work was supported by the National Natural Science Foundation of China under Grant 52107124. Recommended for publication by Associate Editor Q. Shafiee. *(Corresponding author: Zhiguo Hao.)*

Ting Wang, Yanxin Chen, and Zhiguo Hao are with the School of Electrical Engineering, Xi'an Jiaotong University, Xi'an 710049, China (e-mail: wang.ting@xjtu.edu.cn; YanxinChen@stu.xjtu.edu.cn; zhghao@mail.xjtu.edu.cn).

Wei Liu is with NARI Technology Company Ltd., Nanjing 211106, China (e-mail: liuwei13@sgepri.sgcc.com.cn).

Antonello Monti is with the Institute for Automation of Complex Power Systems, E.ON Energy Research Center, RWTH Aachen University, 52074 Aachen, Germany, and also with the Fraunhofer FIT Center for Digital Energy, 52074 Aachen, Germany (e-mail: amonti@eonerc.rwth-aachen.de).

Ferdinanda Ponci is with the Institute for Automation of Complex Power Systems, E.ON Energy Research Center, RWTH Aachen University, 52074 Aachen, Germany (e-mail: fponci@eonerc.rwth-aachen.de).

Color versions of one or more figures in this article are available at https://doi.org/10.1109/TPEL.2025.3595918.

Digital Object Identifier 10.1109/TPEL.2025.3595918

failures [19], [20], [21], [22], [23], line short-circuit faults [22], [23] and sensor faults [24], [25], whereas the observer design for SAFD is not thoroughly studied. In [26], a model-based SAFD method for dc microgrids through estimating system operating states is presented. But this method can only protect the SAFs occurring in load components. Yao et al.[27] presented an observer-based SAFD method for multiterminal dc microgrids, which still have several problems. First of all, this method requires as many full-order observers as protected lines, leading to high computational costs. Second, the applicability of this method is restricted to dc lines with capacitive ends. Third, the selective isolation of faulty lines is based on the smart choice of threshold values, complicating its implementation. Yang et al. [28] proposed a decentralized implementation of the SAFD observers developed in [27], aiming to reduce computational costs. However, the core designs and resulting limitations of the two algorithms remain the same. By comparison, the proposed SAFD method achieves the same fault diagnostic targets using fewer lower-order observers, thus enhancing efficiency. Moreover, it eliminates the reliance on shunt capacitors and avoids individual threshold settings for fault isolation.

From the literature review, we can see that the conventional SAFD methods for dc microgrids suffer from various limitations. To solve all these issues, this article introduces a centralized SAFD method that can simultaneously protect multiple lines in a dc microgrid with reduced-order unknown input observers (ROUIOs). As an effective fault diagnosis approach for complex systems, ROUIOs achieve selective fault isolation through decoupling the influences of selected faults as unknown disturbances [29], [30]. Moreover, since this method involves only a fractional system model in fault diagnostic computation [31], its computational efficiency gets enhanced. In the protection of dc microgrids, ROUIOs have been primarily used for diagnosing switch failures of power electronic converters [32], [33] and short-circuit faults [33], whereas they are designed for SAFD in this work. In this article, a minimized system model of multiterminal dc microgrids tailored for SAFD is first derived. On this basis, a bank of centralized ROUIOs are established in a unified design process. Fault isolation in the proposed SAFD scheme is achieved through identifying predefined fault signatures in the outputs of the ROUIOs. Finally, the effectiveness of the proposed SAFD method as well as its robustness against load disturbances, uncertainties in line parameters and measurement noises are verified with MATLAB/Simulink and hardware.

The major contributions of this work can be synthesized as follows.

1) A centralized SAFD framework based on ROUIO is proposed for dc microgrids. This framework enables the detection and isolation of multiple SAFs in multiterminal dc microgrids without relying on shunt capacitors, auxiliary hardware, special sensors, or prior fault data.
2) The proposed method has an enhanced computational efficiency compared with conventional model-based methods due to its neat design in system modeling and system state decoupling.
3) By eliminating the need for threshold settings in fault isolation, the proposed method not only simplifies implementation but also enhances robustness against modeling uncertainties and measurement noises.

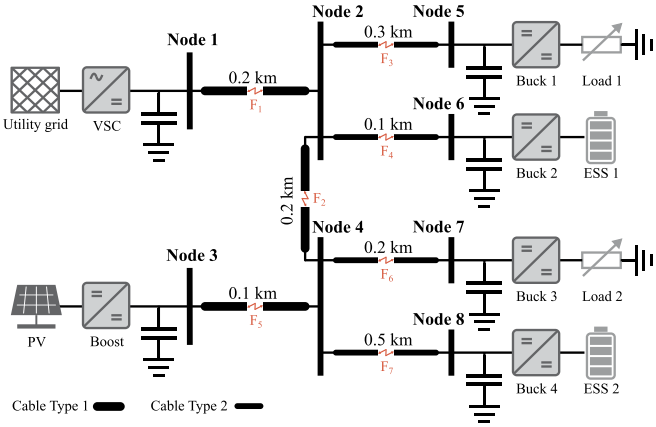

Fig. 1. Reference dc microgrid model.

TABLE I
SYSTEM PARAMETERS

Component	Parameter	Value
VSC	switching frequency rated voltage	1.98 kHz 260 V AC/500 V DC
boost	switching frequency rated voltage	5 kHz 273 V DC/500 V DC
buck	switching frequency rated voltage	10 kHz 500 V DC/200 V DC
cable (Type 1)	resistance per unit length inductance per unit length	0.27 Ω/km 0.29 mH/km
cable (Type 2)	resistance per unit length inductance per unit length	1.16 Ω/km 0.35 mH/km
PV	maximum power	100 kW
load	resistance	10 Ω
ESS	capacity	200 kWh

II. System Overview and Problem Formulation

A. DC Microgrid Model

The study case of dc microgrids is shown in Fig. 1, whose parameters are listed in Table I. The system includes two independent power sources: a three-phase voltage-source converter (VSC) connecting the ac utility grid to Node 1, and a boost converter integrating a photovoltaic (PV) array at Node 3. On the load side, two resistive loads and two ESSs are supplied through buck converters at Nodes 5, 6, 7, and 8. Nodes 2 and 4 serve as intermediate nodes linking the power sources to the load components. The dc microgrid comprises seven dc cables with two ratings (Type 1 and Type 2). The SAF occurring in each dc cable is denoted as F_h $(h = 1, 2, \ldots, 7)$.

B. Problem Formulation

In the multiterminal dc network illustrated in Fig. 1, SAFs can occur in any dc lines. Under such conditions, conventional SAFD

methods designed for single dc branches are unsuitable, as they are highly susceptible to SAF-induced disturbances in adjacent lines. Furthermore, due to the absence of shunt capacitors—commonly used to filter high-frequency components—at Nodes 2 and 4, arc noise generated by SAFs in this grid can propagate into neighboring lines. Hence, traditional SAFD approaches that rely on capacitive terminations at line ends are also inapplicable.

To address these challenges, we propose a centralized scheme that can detect and isolate different SAFs in a multiterminal dc microgrid in one go. The proposed centralized scheme makes use of line currents and node voltages. Besides, only line impedances in the protected dc microgrid are required to design the proposed SAFD algorithm.

III. Modeling of DC Microgrids

A. Representation of System Topology

The topology of a dc microgrid consisting of N nodes and H lines can be represented by an undirected graph denoted as $\mathcal{G} = \{\mathcal{N}, \mathcal{E}\}$. Here, $\mathcal{N} = \{1, 2, \ldots, N\}$ denotes the set of nodes, and $\mathcal{E} = \{(p, q), \ldots, (P, Q)\}$, where (p, q) and (P, Q) denote the set of edges (lines) $(p, q, P, Q \in \mathcal{N})$. For an undirected graph where (p, q) equals (q, p), we will consistently denote a line as (p, q) where $p < q$ [27]. The connection relationships between all dc lines can be represented by a transition matrix denoted as $\theta \in \mathbb{R}^{H\times N}$. For a dc Line (p, q), the pth column and the qth column of a row in θ are 1 and -1, respectively, while all other elements in that row are 0.

B. System Model

The proposed method requires the actual mathematical model of protected system, incorporating both system topologies and cable data. In this work, we intentionally limit the scope of system modeling to the protected dc lines, excluding components installed at dc busbars, such as shunt capacitors and converters. This simplification minimizes the rank of the system model, thereby improving the computational efficiency of the proposed SAFD method. In addition, by eliminating the dependency on shunt capacitors and the operational characteristics of converters, the proposed method achieves greater versatility across various dc microgrids.

Although shunt capacitors and converters are excluded in model parameters, their effects on the system are not neglected. The dynamics induced by these components are captured through changes in node voltages, which are used as input signals to the system model.

The dynamics of a dc microgrid can be expressed as follows:

$$\begin{cases} \dot{x} = Ax + Bu + Ef \\ y = Cx \end{cases} \tag{1}$$

in which u, f, x, and y denote the input vector, the fault vector, the state vector, and the output vector, respectively. A, B, C, and E are parametric matrices.

In this work, u and x are the node voltages and line currents in the monitored dc network, respectively, i.e.,

$$u = \begin{bmatrix} v_1 & \ldots & v_N \end{bmatrix}^{\mathrm{T}} \tag{2}$$

$$x = \begin{bmatrix} i_{(p,q)} & \ldots & i_{(P,Q)} \end{bmatrix}^{\mathrm{T}}. \tag{3}$$

The A and B matrices are determined by line impedance

$$A = \operatorname{diag}\left(-\frac{R_{(p,q)}}{L_{(p,q)}} \quad \ldots \quad -\frac{R_{(P,Q)}}{L_{(P,Q)}} \right) \tag{4}$$

where $R_{(p,q)}$ and $L_{(p,q)}$ denote the resistance and inductance of Line (p, q), respectively.

$$B = \gamma\theta \tag{5}$$

in which

$$\gamma = \operatorname{diag}\left(\frac{1}{L_{(p,q)}} \quad \cdots \quad \frac{1}{L_{(P,Q)}} \right). \tag{6}$$

The C matrix is dependent on the selection of output signals in y. The representations of E and f will be elaborated in Section III-D.

C. Modeling of Fault-Free System

The dc microgrid shown in Fig. 1 contains eight nodes and seven lines, whose topology can be described as $\mathcal{N} = \{1, 2, 3, 4, 5, 6, 7, 8\}$ and $\mathcal{E} = \{(1, 2), (2, 4), (2, 5), (2, 6), (3, 4), (4, 7), (4, 8)\}$. In fault-free ($f = 0$) conditions, the state-space model (1) of this dc microgrid can be defined with the following information:

$$u = \begin{bmatrix} v_1 & v_2 & v_3 & v_4 & v_5 & v_6 & v_7 & v_8 \end{bmatrix}^{\mathrm{T}} \tag{7}$$

$$x = \begin{bmatrix} i_{(1,2)} & i_{(2,4)} & i_{(2,5)} & i_{(2,6)} & i_{(3,4)} & i_{(4,7)} & i_{(4,8)} \end{bmatrix}^{\mathrm{T}} \tag{8}$$

$$A = \operatorname{diag}\left(-\frac{R_{(1,2)}}{L_{(1,2)}} - \frac{R_{(2,4)}}{L_{(2,4)}} - \frac{R_{(2,5)}}{L_{(2,5)}} - \frac{R_{(2,6)}}{L_{(2,6)}} - \frac{R_{(3,4)}}{L_{(3,4)}} - \frac{R_{(4,7)}}{L_{(4,7)}} - \frac{R_{(4,8)}}{L_{(4,8)}} \right) \tag{9}$$

$$B = \gamma\theta = \begin{bmatrix} \frac{1}{L_{(1,2)}} & \frac{-1}{L_{(1,2)}} & 0 & 0 & 0 & 0 & 0 & 0 \\ 0 & \frac{1}{L_{(2,4)}} & 0 & \frac{-1}{L_{(2,4)}} & 0 & 0 & 0 & 0 \\ 0 & \frac{1}{L_{(2,5)}} & 0 & 0 & \frac{-1}{L_{(2,5)}} & 0 & 0 & 0 \\ 0 & \frac{1}{L_{(2,6)}} & 0 & 0 & 0 & \frac{-1}{L_{(2,6)}} & 0 & 0 \\ 0 & 0 & \frac{1}{L_{(3,4)}} & \frac{-1}{L_{(3,4)}} & 0 & 0 & 0 & 0 \\ 0 & 0 & 0 & \frac{1}{L_{(4,7)}} & 0 & 0 & \frac{-1}{L_{(4,7)}} & 0 \\ 0 & 0 & 0 & \frac{1}{L_{(4,8)}} & 0 & 0 & 0 & \frac{-1}{L_{(4,8)}} \end{bmatrix} \tag{10}$$

where

$\gamma =$

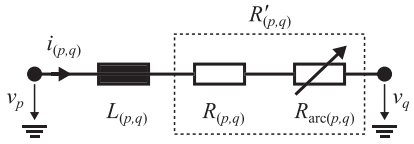

Fig. 2. Equivalent circuit model of a dc line with an SAF.

$$\mathrm{diag}\left(\frac{1}{L_{(1,2)}} \quad \frac{1}{L_{(2,4)}} \quad \frac{1}{L_{(2,5)}} \quad \frac{1}{L_{(2,6)}} \quad \frac{1}{L_{(3,4)}} \quad \frac{1}{L_{(4,7)}} \quad \frac{1}{L_{(4,8)}}\right) \tag{11}$$

$$\theta = \begin{bmatrix} 1 & -1 & 0 & 0 & 0 & 0 & 0 & 0 \\ 0 & 1 & 0 & -1 & 0 & 0 & 0 & 0 \\ 0 & 1 & 0 & 0 & -1 & 0 & 0 & 0 \\ 0 & 1 & 0 & 0 & 0 & -1 & 0 & 0 \\ 0 & 0 & 1 & -1 & 0 & 0 & 0 & 0 \\ 0 & 0 & 0 & 1 & 0 & 0 & -1 & 0 \\ 0 & 0 & 0 & 1 & 0 & 0 & 0 & -1 \end{bmatrix}. \tag{12}$$

For simplicity, C is set to be an identity matrix, so

$$y = x. \tag{13}$$

D. Modeling of SAF

As detailed in [34], the effect of an SAF can be effectively modeled as a time-varying resistance. Leveraging this principle, we constructed the equivalent circuit of a dc line experiencing an SAF, as depicted in Fig. 2. The figure highlights that an SAF in Line (p, q) manifests as an unexpected increase in the line resistance $R_{(p,q)}$, represented by an additional arc resistance $R_{\mathrm{arc}(p,q)}$. This effect of SAF on line resistance is expressed as

$$R_{(p,q)} \to R'_{(p,q)} = R_{(p,q)} + R_{\mathrm{arc}(p,q)}. \tag{14}$$

This representation provides a clear foundation for analyzing the impacts of SAFs on the dynamic behavior in the dc microgrid. By integrating the expression of the SAF (14) into the system model (1), an analytical model of the SAF can be obtained.

Taking F_1 in Line (1,2) in the reference dc microgrid as an example to clarify the mathematical modeling of SAFs. Replacing $R_{(1,2)}$ with $R_{(1,2)} + R_{\mathrm{arc}(1,2)}$ in the state-space equation of the system model (1) yields (Due to space limitation, only the state-space equation that is relevant to the modeling of F_1 is presented)

$$\underbrace{\dot{i}_{(1,2)}}_{\dot{x}} = \underbrace{-\frac{R_{(1,2)}}{L_{(1,2)}} i_{(1,2)}}_{Ax} + \underbrace{\frac{1}{L_{(1,2)}}(v_1 - v_2)}_{Bu} \underbrace{-\frac{1}{L_{(1,2)}}}_{E} \underbrace{R_{\mathrm{arc}(1,2)} i_{(1,2)}}_{f}. \tag{15}$$

From (15), the expressions of E and f for F_1 can be derived. The mathematical models of other SAFs can be derived in the same process. E and f for all the seven SAFs in the reference dc microgrid are summarized in Table II.

TABLE II
SAF MODELS

SAF	Line	E	f
F_1	$(1,2)$	$\left[\frac{-1}{L_{(1,2)}} \ 0 \ 0 \ 0 \ 0 \ 0 \ 0\right]^{\mathrm{T}}$	$R_{\mathrm{arc}(1,2)} i_{(1,2)}$
F_2	$(2,4)$	$\left[0 \ \frac{-1}{L_{(2,4)}} \ 0 \ 0 \ 0 \ 0 \ 0\right]^{\mathrm{T}}$	$R_{\mathrm{arc}(2,4)} i_{(2,4)}$
F_3	$(2,5)$	$\left[0 \ 0 \ \frac{-1}{L_{(2,5)}} \ 0 \ 0 \ 0 \ 0\right]^{\mathrm{T}}$	$R_{\mathrm{arc}(2,5)} i_{(2,5)}$
F_4	$(2,6)$	$\left[0 \ 0 \ 0 \ \frac{-1}{L_{(2,6)}} \ 0 \ 0 \ 0\right]^{\mathrm{T}}$	$R_{\mathrm{arc}(2,6)} i_{(2,6)}$
F_5	$(3,4)$	$\left[0 \ 0 \ 0 \ 0 \ \frac{-1}{L_{(3,4)}} \ 0 \ 0\right]^{\mathrm{T}}$	$R_{\mathrm{arc}(3,4)} i_{(3,4)}$
F_6	$(4,7)$	$\left[0 \ 0 \ 0 \ 0 \ 0 \ \frac{-1}{L_{(4,7)}} \ 0\right]^{\mathrm{T}}$	$R_{\mathrm{arc}(4,7)} i_{(4,7)}$
F_7	$(4,8)$	$\left[0 \ 0 \ 0 \ 0 \ 0 \ 0 \ \frac{-1}{L_{(4,8)}}\right]^{\mathrm{T}}$	$R_{\mathrm{arc}(4,8)} i_{(4,8)}$

TABLE III
SENSITIVITY MATRIX

	F_1	F_2	F_3	F_4	F_5	F_6	F_7
Observer 1	1	0	1	0	1	0	1
Observer 2	0	1	1	0	0	1	1
Observer 3	0	0	0	1	1	1	1

IV. SAFD METHOD

This section explains the designs of observers and the fault signature recognition scheme in the proposed SAFD method, whereafter, a complete workflow is presented.

A. Observer Bank Design

To simultaneously diagnose multiple SAFs in a dc microgrid, a bank of multiple observers with individual fault diagnostic targets are designed. Instead of using as many observers as protected lines, this work employs a highly efficient design scheme, in which the number M of observers required to cover H independent faults is determined as [22]

$$M \geq \lceil \log_2 (H + 1) \rceil. \tag{16}$$

To ensure the selectivity of protection, each observer must be designed to be sensitive only to specific faults, while treating other faults as disturbances. The sensitivities of M observers to H faults can be represented by a sensitivity matrix $S \in \mathbb{R}^{M \times H}$. The elements in S are defined by

$$S_{mh} = \begin{cases} 1, & \text{if Observer } m \text{ is sensitive to Fault } h \\ 0, & \text{if Observer } m \text{ is insensitive to Fault } h \end{cases} \tag{17}$$

where $m = 1, 2, \ldots, M$, $h = 1, 2, \ldots, H$. Each column of S represents the sensitivities of the M observers to a fault, which is referred to as a fault signature. The elements in the sensitivity matrix can be freely determined as long as all fault signatures are unique.

To detect all the seven SAFs in the reference dc microgrid, only three observers are enough according to (16). The sensitivity matrix of this observer bank is represented in Table III.

In this sensitivity matrix, each column is a unique three-digit vector, which guarantees the selectivity in SAFD.

B. ROUIO Design

With the sensitivity of an ROUIO determined, its parameters can be designed in the process described in [35], which is explained in the following.

Taking into account the target of SAFD, the system model (1) can be rewritten as

$$\begin{cases} \dot{x} = Ax + Bu + E_1 f_1 + E_2 f_2 \\ y = Cx \end{cases} \tag{18}$$

in which $\{E_1, f_1\}$ corresponds to the faults to which the observer is insensitive, and $\{E_2, f_2\}$ corresponds to the faults to which the observer should respond. Discretizing (18) yields

$$\begin{cases} x(k+1) = A_\mathrm{d} x(k) + B_\mathrm{d} u(k) + E_{\mathrm{d},1} f_1(k) + E_{\mathrm{d},2} f_2(k) \\ y(k) = C_\mathrm{d} x(k) \end{cases}. \tag{19}$$

Applying state transformation $z = Tx$ on (19) yields

$$\begin{cases} z(k+1) = TA_\mathrm{d}T^{-1} z(k) + TB_\mathrm{d} u(k) + TE_{\mathrm{d},1} f_1(k) \\ \qquad\qquad + TE_{\mathrm{d},2} f_2(k) \\ y(k) = C_\mathrm{d} T^{-1} z(k) \end{cases} \tag{20}$$

where the nonsingular matrix $T = U_1^\mathrm{T}$, and U_1 is obtained from the singular value decomposition (SVD) of $E_{\mathrm{d},1}$:

$$E_{\mathrm{d},1} = U_1 \begin{bmatrix} \Sigma_1 \\ 0 \end{bmatrix} V_1^\mathrm{T}. \tag{21}$$

The transformed system model (20) can be split into

$$z_1(k+1) = A_{11} z_1(k) + A_{12} z_2(k) + B_1 u(k) + E_{11} f_1(k) + E_{21} f_2(k) \tag{22}$$

$$z_2(k+1) = A_{21} z_1(k) + A_{22} z_2(k) + B_2 u(k) + E_{22} f_2(k) \tag{23}$$

$$y(k) = C_1 z_1(k) + C_2 z_2(k) \tag{24}$$

in which the following relationships exist:

$$TA_\mathrm{d}T^{-1} = \begin{bmatrix} A_{11} & A_{12} \\ A_{21} & A_{22} \end{bmatrix} \tag{25}$$

$$TB_\mathrm{d} = \begin{bmatrix} B_1 & B_2 \end{bmatrix}^\mathrm{T} \tag{26}$$

$$C_\mathrm{d}T^{-1} = \begin{bmatrix} C_1 & C_2 \end{bmatrix} \tag{27}$$

$$TE_{\mathrm{d},1} = \begin{bmatrix} E_{11} & 0 \end{bmatrix}^\mathrm{T} \tag{28}$$

$$TE_{\mathrm{d},2} = \begin{bmatrix} E_{21} & E_{22} \end{bmatrix}^\mathrm{T}. \tag{29}$$

Applying output transformation on (24) yields

$$y^\star(k) = T_1 y(k) \tag{30}$$

where $T_1 = U_2^\mathrm{T}$. The SVD of C_1 results in U_2:

$$C_1 = U_2 \begin{bmatrix} \Sigma_2 \\ 0 \end{bmatrix} V_2^\mathrm{T}. \tag{31}$$

By partitioning $y^\star(k)$ into $[y_1^\star(k) \;\; y_2^\star(k)]^\mathrm{T}$ and $T_1 C_2$ into $[C_{21} \;\; C_{22}]^\mathrm{T}$, (30) can be expressed in a modified form:

$$y_1^\star(k) = \Sigma_2 V_2^\mathrm{T} z_1(k) + C_{21} z_2(k) \tag{32}$$

$$y_2^\star(k) = C_{22} z_2(k). \tag{33}$$

Substituting $z_1(k)$ from (32) into (23) yields

$$\begin{cases} z_2(k+1) = \bar{A}_{22} z_2(k) + B_2 u(k) \\ \qquad\qquad + A_{21} (\Sigma_2 V_2^\mathrm{T})^+ y_1^\star(k) + E_{22} f_2(k) \\ y_2^\star(k) = C_{22} z_2(k) \end{cases} \tag{34}$$

where $\bar{A}_{22} = A_{22} - A_{21}(\Sigma_2 V_2^\mathrm{T})^+ C_{21}$ and $()^+$ denotes the Moore–Penrose pseudoinverse.

Equation (34) is the reduced system model for ROUIO design. Its rank n_2 is determined by

$$n_2 = n_\mathrm{s} - \mathrm{rank}(E_{\mathrm{d},1}) \tag{35}$$

which is lower than the rank n_s of original system model (19). The necessary and sufficient conditions for the existence of an ROUIO for the system defined by (19) are [36]

1) $\mathrm{rank}(CE_{\mathrm{d},1}) = \mathrm{rank}(E_{\mathrm{d},1})$.
2) $(C_{22}, \bar{A}_{22})$ is a detectable pair.

Based on the reduced-order system model (34), the ROUIO can be expressed as

$$\begin{cases} \hat{z}_2(k+1) = (\bar{A}_{22} - WC_{22})\hat{z}_2(k) + B_2 u(k) \\ \qquad\qquad + A_{21}(\Sigma_2 V_2^\mathrm{T})^+ y_1^\star(k) + W y_2^\star(k) \\ r(k) = y_2^\star(k) - C_{22}\hat{z}_2(k) \end{cases} \tag{36}$$

in which r is the residual generated by the ROUIO.

C. Order Analysis

The reduction of observer complexity is accomplished through the elimination of system states that are irrelevant to fault diagnosis, as detailed in the following.

As demonstrated in Section IV-B, the transformed state-space representation of the dynamic system (20) can be decomposed into two subsystems described by (22) and (23), respectively. The state vector z_1 in (22) is influenced by both disturbances f_1 and faults f_2, while z_2 in (23) is affected only by faults f_2. This allows fault diagnosis to rely solely on the reduced-order subsystem (23). The resulting reduced-order model (34) retains only z_2, forming the basis for ROUIO design.

The order reduction mechanism is quantitatively characterized by the relationship established in (35). Since n_s remains constant for an system, n_2 exhibits an inverse relationship with the number ($\mathrm{rank}(E_{\mathrm{d},1})$) of disturbances. This means that n_2 is an adjustable parameter tailored to the specific fault diagnostic target of the observer. Specifically, as more faults are treated as disturbances by an ROUIO, its rank n_2 decreases accordingly. But as $\mathrm{rank}(E_{\mathrm{d},1})$ is a positive value below n_s, the rank of

ROUIO is always lower than the order of the original system model.

D. Signature Recognition Scheme

This section introduces a signature recognition scheme that locates faulty lines based on the residual norms generated by the ROUIO bank.

Let r_m denote the residual generated by the mth observer in the bank of M ROUIOs ($m = 1, 2, \ldots, M$). The L^2 norm of r_m can be represented as

$$J_m(k) = \| r_m(k) \| = \sqrt{r_m(k)^{\mathrm{T}} r_m(k)}. \tag{37}$$

The SAFD function is triggered when the residual norm generated by any observer consistently exceeds its corresponding threshold for a certain duration, i.e., if $\exists\, m \in [1, 2, \ldots, M]$ such that

$$J_m(k) > J_{m,\mathrm{th}},\ k = 1, 2, \ldots, K \tag{38}$$

where the threshold $J_{m,\mathrm{th}}$ is set to avoid the maximum error in J_m in fault-free ($f = 0$) operating conditions. It should be noted that $J_{m,\mathrm{th}}$ is a fixed value for a specific observer, which is independent of faults to detect.

The selection of data length K is critical as it directly affects the response time of the SAFD function. The UL 1699B standard allows for 2 s for arc interruption [37], [38]. In our work, we choose K to correspond to a sampling delay of only 10 ms. This choice guarantees the fast response of the proposed SAFD method in the early phase of SAFs.

First, all the M obtained residual norms are normalized:

$$J_m^{\mathrm{N}}(k) = \frac{J_m(k)}{\max\{J_1(k), J_2(k), \ldots, J_M(k)\}}. \tag{39}$$

Through the observer parameter design, multiple ROUIOs sensitive to the same fault generate identical residuals. By normalizing these residuals, each residual norm is converted into a binary output: 1 (indicating that the corresponding observer is sensitive to the fault) or 0 (indicating insensitivity to the fault). In such a way, an M-digit binary vector can be obtained through normalizing the residual norms of all the M observers, which should match a predefined fault signature. Therefore, the task of SAFD becomes the recognition of predefined binary patterns in the normalized residual norms.

To identify the fault signature that best matches the binary pattern in the normalized residual norms, the Euclidean distance between the normalized residual norms $J^{\mathrm{N}}(k) = [J_1^{\mathrm{N}}(k) \quad J_2^{\mathrm{N}}(k) \quad \ldots \quad J_M^{\mathrm{N}}(k)]^{\mathrm{T}}$ and the fault signature $S_h = [S_{1h} \quad S_{2h} \quad \ldots \quad S_{Mh}]^{\mathrm{T}}$ of F_h is calculated

$$E_h(k) = \| J^{\mathrm{N}}(k) - S_h \|. \tag{40}$$

E_h represents the error in reconstructing the fault signature S_h from the normalized residual norms.

Then, the mean value of the reconstruction error over the sampling period is calculated

$$\bar{E}_h = \frac{1}{K} \sum_{k=1}^{K} E_h(k). \tag{41}$$

TABLE IV
MEAN RECONSTRUCTION ERRORS IN DIFFERENT FAULT SCENARIOS

Fault	$\bar{E}_1$	$\bar{E}_2$	$\bar{E}_3$	$\bar{E}_4$	$\bar{E}_5$	$\bar{E}_6$	$\bar{E}_7$
F_1	**0.108**	1.379	0.950	1.352	0.910	1.648	1.310
F_2	1.377	**0.090**	0.947	1.366	1.659	0.931	1.324
F_3	1.003	1.005	**0.095**	1.676	1.346	1.348	0.904
F_4	1.387	1.393	1.692	**0.048**	0.963	0.971	1.366
F_5	1.000	1.714	1.393	0.999	**0.028**	1.392	0.971
F_6	1.703	1.001	1.381	0.999	1.379	**0.046**	0.953
F_7	1.411	1.412	0.999	1.410	0.996	0.998	**0.004**

By finding the argument x of the minimum $\bar{E}_h$ ($h = 1, 2, \ldots, H$), the signature of fault F_x can be recognized without using any threshold values.

E. Workflow of SAFD Scheme

The complete workflow of the proposed SAFD process is shown in Fig. 3, which can be divided into two blocks named "Observer bank" and "Fault signature recognition." In the "Observer bank," multiple ROUIOs are implemented in parallel, sharing the common measurement signals u and y. The internal parameters of each ROUIO are designed in the generic process presented in Section IV-B. The "Fault signature recognition" is triggered if the condition (38) is satisfied, then the mean reconstruction errors are calculated with the residuals generated by the observer bank. Through finding the argument $x = \arg\min_h \bar{E}_h$ ($h = 1, 2, \ldots, H$), the faulty line with SAF can be recognized.

V. NUMERICAL SIMULATIONS

In this section, the performance of the proposed SAFD method is tested in different fault scenarios in the reference dc microgrid through simulations with MATLAB/Simulink. Then, its robustness against load disturbances, modeling errors and measurement noises is verified.

A. Performance Verification

To verify the effectiveness of the proposed method, it was first tested under different SAFs in the reference dc microgrid.

Fig. 4 presents the test results under SAF F_1. We can see that after the SAF occurs at 50 ms, J_1 increases rapidly and stabilizes at a high level, whereas J_2 and J_3 fluctuate at low levels. This result aligns with theoretical analysis. According to the signature of F_1 in the predefined sensitivity matrix (shown in Table III), Observer 1 is sensitive to F_1, and Observer 2 and Observer 3 are insensitive to F_1.

Moreover, Fig. 4(b) presents the reconstruction errors under F_1, we can see that E_1 is much lower than all the other six reconstruction errors. This indicates that the pattern in the residual norms generated by the observer bank most closely matches to the signature of F_1.

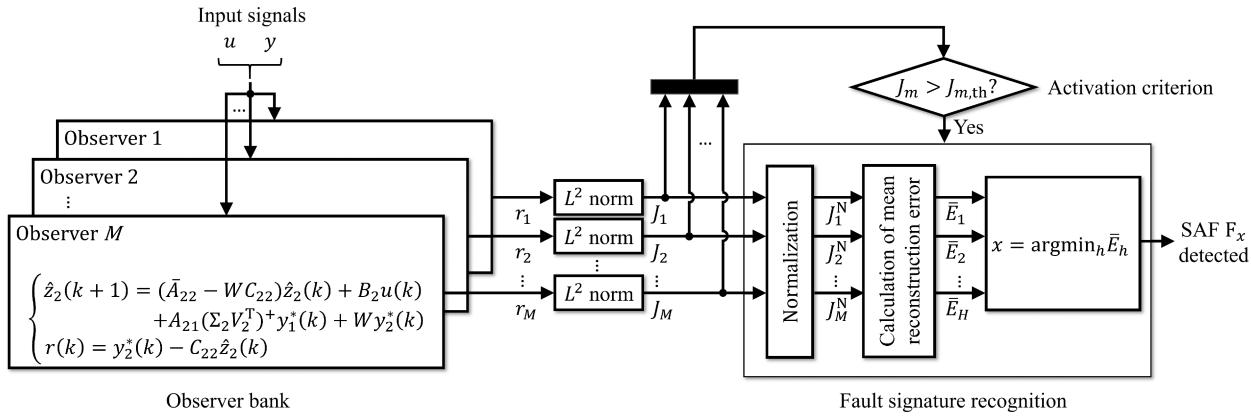

Fig. 3. Workflow of the proposed SAFD method.

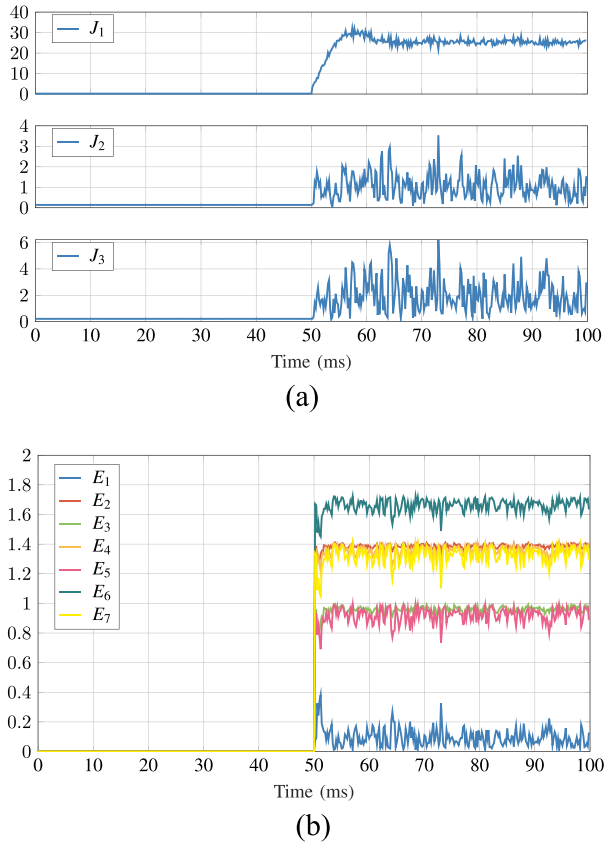

Fig. 4. (a) Residual norms and (b) reconstruction errors during the SAF F_1.

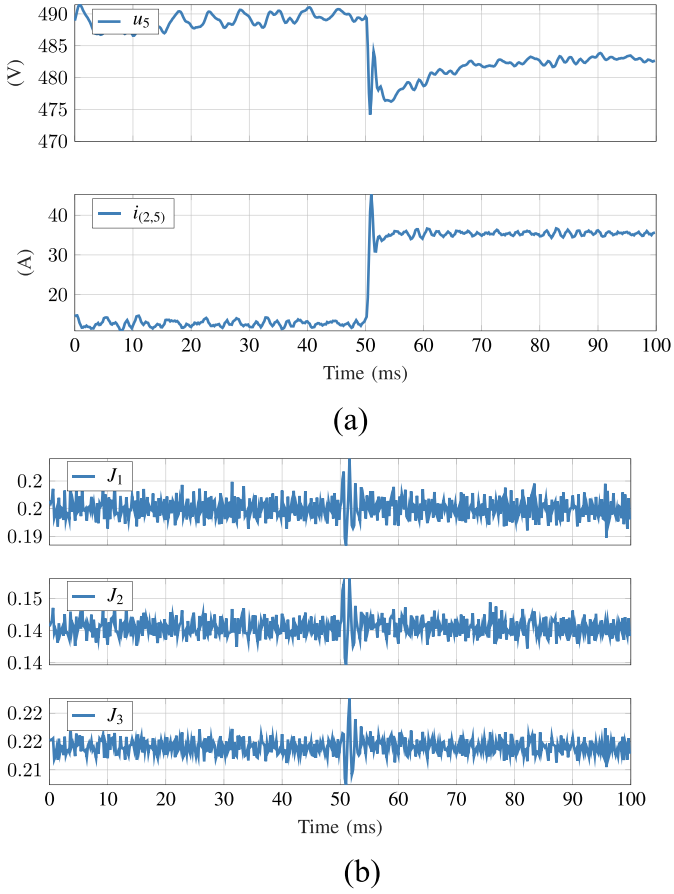

Fig. 5. (a) Node voltage and line current, and (b) residual norms during the abrupt change in Load 1.

Table IV presents the mean reconstruction errors obtained under all the seven SAFs in the reference dc microgrid. As we can see, the mean reconstruction errors $\bar{E}_h$ associated with F_h $(h = 1, 2, \ldots, 7)$ are always the lowest. Therefore, through finding the minimum mean reconstruction errors, the different SAFs can be recognized without using any thresholds.

B. Robustness Verification

1) Influence of Load Disturbances: To induce load disturbances in the reference dc microgrid, we simulated a sudden increase in Load 1 at Node 5, which is fed via Line (2,5). The voltage of Node 5, the current in Line (2,5), and the residual norms during this disturbance are plotted in Fig. 5.

Fig. 5(a) shows that the load change (at 50 ms) leads to abrupt changes in the line current $i_{(2,5)}$ and the node voltage u_5. In the meantime, the residual norms J_1, J_2, and J_3 experience only transient fluctuations during the load change. Since there is no steady deviation in the three residual norms [see Fig. 5(b)], the proposed SAFD function is not activated.

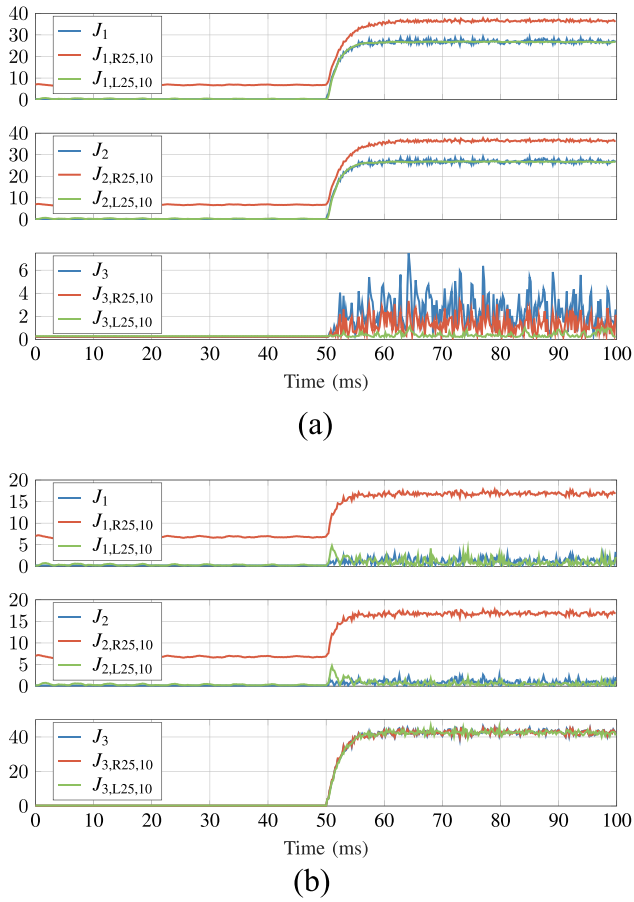

Fig. 6. Residual norms during (a) the SAF F_3 and (b) the SAF F_4 under different modeling errors in Line (2,5).

TABLE V
MEAN RECONSTRUCTION ERRORS UNDER MODELING ERRORS

Fault	$\bar{E}_1$	$\bar{E}_2$	$\bar{E}_3$	$\bar{E}_4$	$\bar{E}_5$	$\bar{E}_6$	$\bar{E}_7$
F_3	1.003	1.005	**0.095**	1.676	1.346	1.348	0.904
$F_{3,R25,10}$	1.000	1.000	**0.038**	1.709	1.386	1.386	0.961
$F_{3,L25,10}$	0.999	0.999	**0.018**	1.720	1.401	1.401	0.981
F_4	1.387	1.393	1.692	**0.048**	0.963	0.971	1.366
$F_{4,R25,10}$	1.231	1.232	1.301	**0.582**	0.719	0.719	0.832
$F_{4,L25,10}$	1.371	1.376	1.656	**0.097**	0.936	0.943	1.317

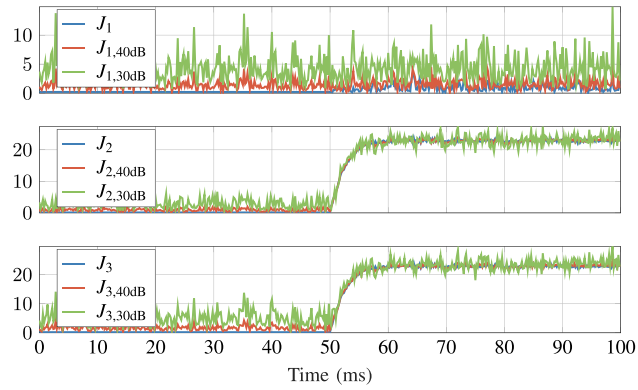

Fig. 7. Residual norms during the SAF F_6 under different measurement noises.

The good robustness of the proposed method against load changes can be explained by the fact that the load change only affects node voltages, which are the input variables in the system model (1). Since the SAFs are modeled as the parametric changes in the system model (1), they are irrelevant to input values. Due to this reason, the proposed method is insensitive to changes in operating environment.

2) Influence of Modeling Errors: To verify the influence of the inaccuracy in line parameters on the performance of the proposed method, we created extreme modeling errors by individually increasing the resistance and inductance of Line (2,5) in the simulation model by ten times, while keeping the parameters of ROUIOs unchanged. Under the influences of the modeling errors, the proposed method is tested under F_3 occurring in Line (2,5) and F_4 occurring in its neighboring Line (2,6), respectively.

In Fig. 6, the original residual norms without modeling errors are denoted by J_m ($m = 1, 2, 3$), while $J_{m,R25,10}$ ($m = 1, 2, 3$) and $J_{m,L25,10}$ ($m = 1, 2, 3$) denote the residual norms obtained under the resistive and the inductive modeling errors in Line (2,5), respectively. As shown in Fig. 6(a) and (b), resistive modeling errors in the protected Line (2,5) cause dc deviations in the residual norms $J_{m,R25,10}$ ($m = 1, 2$), whereas inductive errors only smooth out the fluctuations in residual norms $J_{m,L25,10}$ ($m = 1, 2, 3$). However, as we can see in Table V, even under the severe modeling errors (900% relative error), the mean reconstruction errors $\bar{E}_3$ and $\bar{E}_4$ are still the lowest under F_3 and F_4, respectively, which guarantee correct fault diagnostic results. These results prove the good robustness of the proposed SAFD method against modeling uncertainty.

The robustness of the proposed method can be attributed to the normalization of the residual norms. Although resistive modeling errors can lead to deviations in residual norms, these changes are still minor compared to those caused by SAFs. Through the normalization of residual norms, the influences of the modeling errors are effectively scaled down. As a result, the functioning of the proposed method is not affected.

3) Influence of Measurement Noises: To evaluate the performance of the proposed method in noisy measurement conditions, it was tested under F_6 in the reference dc microgrid with additional white Gaussian noises in the measurement signals.

Fig. 7 plots the original residual norms without measurement noises (J_m, $m = 1, 2, 3$), as well as the residual norms obtained under the measurement noises of 40 dB ($J_{m,40dB}$, $m = 1, 2, 3$) and 30 dB ($J_{m,30dB}$, $m = 1, 2, 3$), respectively. We can see that as the magnitudes of the additional measurement noises increase, the fluctuations in the obtained residual norms become more significant. Nevertheless, even under the most extreme noises of 30 dB, the fault signature $[0 \quad 1 \quad 1]^T$ in the obtained residual norms $J_{m,30dB}$ ($m = 1, 2, 3$) is still salient to recognize.

The quantitative results of the mean reconstruction errors are presented in Table VI. We can see that $\bar{E}_6$ is always the lowest

TABLE VI
MEAN RECONSTRUCTION ERRORS UNDER MEASUREMENT NOISES

Fault	$\bar{E}_1$	$\bar{E}_2$	$\bar{E}_3$	$\bar{E}_4$	$\bar{E}_5$	$\bar{E}_6$	$\bar{E}_7$
F_6	1.703	1.001	1.381	0.999	1.379	**0.046**	0.953
$F_{6,40dB}$	1.659	0.998	1.337	0.989	1.329	**0.097**	0.896
$F_{6,30dB}$	1.591	1.026	1.265	0.996	1.240	**0.224**	0.777

under the different measurement noises. Under the extreme noises of 30 dB, there is still a large margin between $\bar{E}_6$ (0.224) and all other mean reconstruction errors (from 0.777), which proves the good tolerance of the proposed method for measurement noises.

The proposed method exhibits good robustness against measurement noises due to two key factors: normalization of the residual norms and averaging of the reconstruction errors. The normalization of the residual norms significantly reduces the impact of measurement noises by scaling down their magnitudes. The averaging of the reconstruction errors further diminishes the influence of measurement noises since they are zero-mean.

C. Adaptivity in Different System Configurations

To validate the adaptivity of the proposed method in systems with different topologies and cable lengths, the proposed method is also tested in a modified system with the following changes:

1) Node 8 (including Buck 4 converter and ESS 2) is moved from Node 4 to Node 2.
2) The length of new Line (2,8) is increased to 5 km.

In accordance with the updated system configuration, the ROUIO bank is rebuilt. Here, the new SAF occurring in Line (2,8) is defined as F_7 and assigned the signature $[1,1,1]^{\mathrm{T}}$.

The output of the observer bank is presented in Fig. 8. As shown in Fig. 8(a), J_1 to J_3 rise to the same high level after fault occurrence, matching the predefined fault signature $[1,1,1]^{\mathrm{T}}$. Meanwhile, the reconstruction errors in Fig. 8(b) indicate that E_7 is the lowest, confirming the occurrence of F_7. These test results demonstrate that the effectiveness of the proposed method is not limited to a specific scenario but can be extended to dc systems with different topologies and cable lengths.

D. Comparison With Model-Free Methods

To demonstrate the advantageous features of the proposed method over conventional model-free methods, theoretical and numerical comparisons are carried out in the following.

Table VII compares the proposed method with several model-free SAFD methods in different dimensions. As we can see, conventional signal processing methods [2], [3], [4], [5], [6], [7], [8], [9], [10] are not suitable for protecting multiterminal dc microgrids, as they fail to account for the impacts of external SAFs in neighboring lines. Other SAFD methods are deficient in that they rely on additional components, such as shunt capacitors [11], resonant filters [12], specialized sensors [13], [14], or historical operating data [15], [16], [17], reducing their

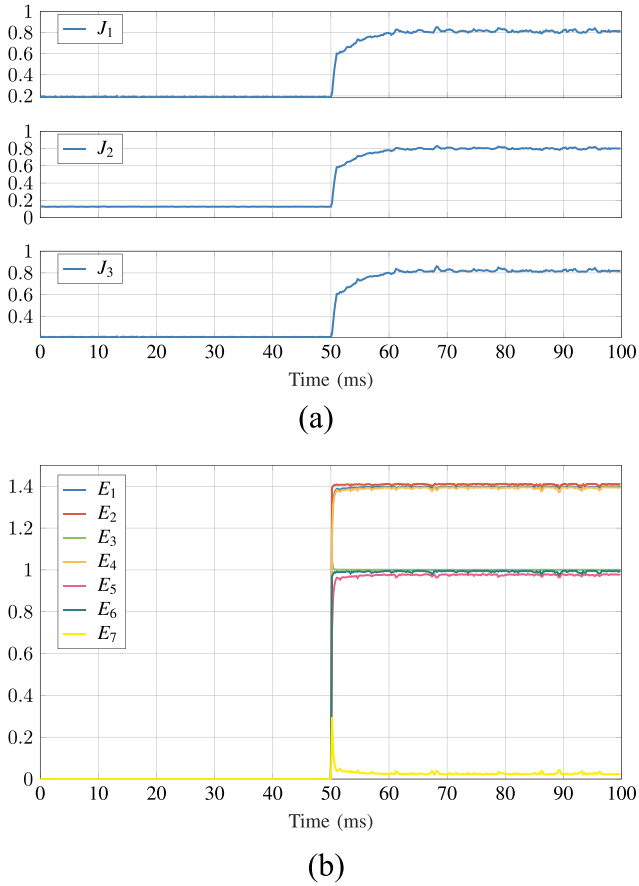

Fig. 8. (a) Residual norms and (b) reconstruction errors during the SAF F_7 under the new system configuration.

TABLE VII
COMPARISON WITH EXISTING METHODS

	single line exclusive	req. shunt capacitors	req. auxiliary hardware	req. special sensors	req. historical fault data	req. threshold setting for fault isolation
time-domain features [2]–[4]	Y	N	N	N	N	Y
statistical features [5]–[7]	Y	N	N	N	N	Y
frequency-domain features [8]–[10]	Y	N	N	N	N	Y
shunt capacitor [11]	N	Y	N	N	N	Y
resonant filter [12]	N	N	Y	N	N	N
non-electric signals [13], [14]	N	N	N	Y	N	Y
data-driven models [15]–[17]	N	N	N	N	Y	N
proposed method	N	N	N	N	N	N

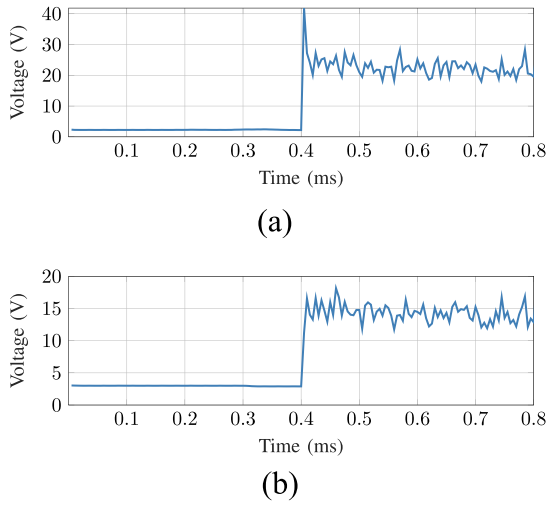

Fig. 9. Standard deviation of voltage difference in (a) Line (2,4) and (b) Line (4,7) during the SAF F_2.

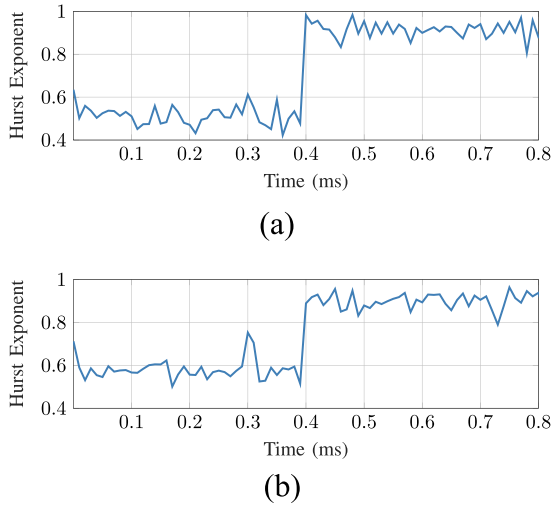

Fig. 10. Hurst exponent of current in (a) Line (2,4) and (b) Line (4,7) during the SAF F_2.

implementation feasibility. Moreover, most of these methods require case-specific threshold tuning for fault isolation. All these limitations are overcome by the proposed method. First, it is designed for protecting multiterminal dc microgrids, extending its applicability beyond single-line protection. Second, its implementation eliminates the need for shunt capacitors, auxiliary hardware, specialized sensors, or historical fault data, as demonstrated in the case study. Third, it isolates faulty dc lines by identifying the minimum reconstruction error, bypassing the challenge of threshold setting.

Besides the theoretical discussion, numerical comparisons are also conducted with the signal processing-based methods presented in [3], [5], [8], [10]. These methods are chosen for comparison because they do not rely on shunt capacitors, auxiliary hardware, specialized sensors, or historical fault data, aligning with the implementation constraints of the proposed method. This ensures a fair and unbiased comparison between the proposed method and the selected alternatives.

In this comparative test, we simulate the SAF F_2 in Line (2,4) and monitor four signal types from Line (2,4) and its adjacent Line (4,7): the standard deviation of voltage difference [3], the Hurst exponent [5], and the Fourier [8] and wavelet components [10] of the line current. The simulation results in Figs. 9–12 demonstrate that the four SAFD reference signals show abrupt increases after fault inception in both the faulted Line (2,4) and its neighboring healthy Line (4,7), reaching values substantially higher than their prefault baselines. Thus, faulty lines can not be isolated simply through comparing prefault and postfault signal amplitudes. For comparison, Fig. 13 presents the outputs of the proposed method under the same fault scenario. The residual norm patterns in Fig. 13(a) demonstrate that during the SAF F_2, J_2 becomes dominant while J_1 and J_3 maintain low values, consistent with the predefined signature of F_2 in Table III. Furthermore, the reconstruction errors shown in Fig. 13(b) reveal successful E_2 minimization for F_2, enabling accurate SAFD through minimum-error identification.

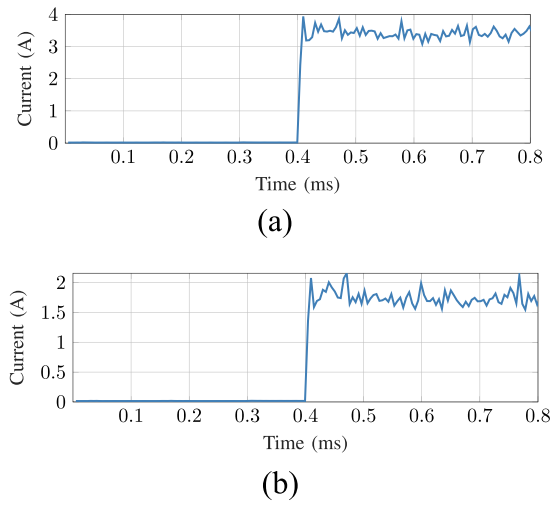

Fig. 11. Fourier components of currents in (a) Line (2,4) and (b) Line (4,7) during the SAF F_2.

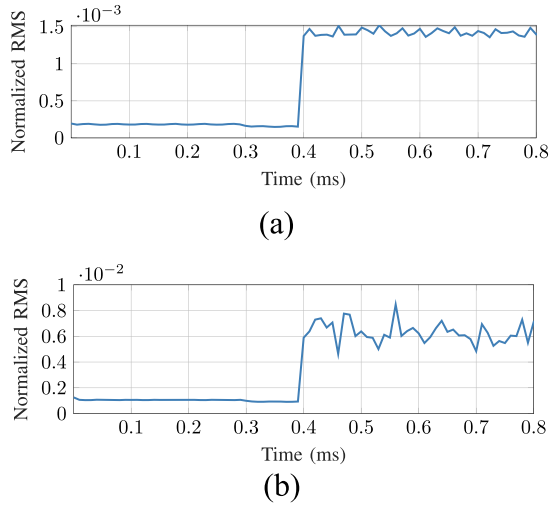

Fig. 12. wavelet components of currents in (a) Line (2,4) and (b) Line (4,7) during the SAF F_2.

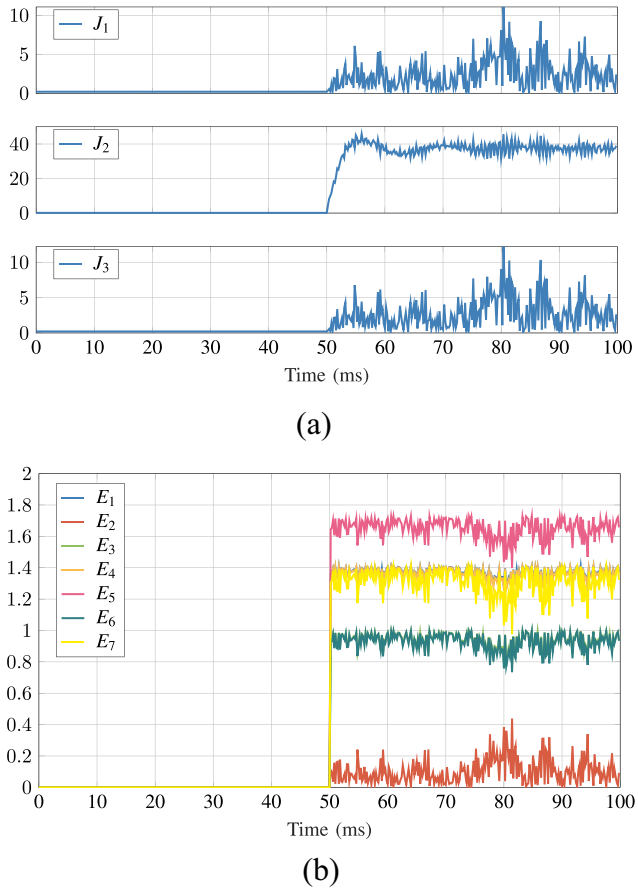

Fig. 13. (a) Residual norms and (b) reconstruction errors during the SAF F_2.

The superiority of the proposed model-based method stems from the following key characteristics that address the inherent limitations of model-free techniques:

1) Unlike signal processing-based methods that can fail under arc-induced disturbances, the proposed method embeds the mathematical model of system dynamics. By observing system operating states and verifying their consistency with physical laws, it pinpoints the fault location that best explains the observed dynamics, thereby requiring no additional sensors, dedicated hardware, or case-specific threshold tuning.
2) Unlike data-driven methods, the proposed method detects SAFs based on first-principle system models. This property ensures its validity across unseen operating conditions without requiring fault databases for training.

E. Comparison With Model-Based Methods

While model-based SAFD methods remain relatively scarce in the literature, the proposed method demonstrates significant advancements over existing approaches, particularly the notable work of [27] as one of the few comparable studies, with marked improvements in computational efficiency and practical applicability, as will be detailed subsequently.

1) Efficiency: The computational load of observer-based systems is jointly determined by both the quantity of observers and their individual orders. And the proposed SAFD method achieves enhanced efficiency through limiting both the number and the ranks of observers involved in fault diagnostic computations, which is explained in the following.

The first improvement in the proposed method lies on a multifault diagnostic framework, enabling a single observer to concurrently monitor and identify multiple SAFs across various dc lines. According to (16), the minimum number of observers required in the proposed method to cover H independent faults is as low as $\lceil \log_2 (H+1) \rceil$. This represents a substantial enhancement compared to the conventional approach in [27], which requires a dedicated observer for each individual line protection.

The second improvement in our work is the reduction of observer order through two key mechanisms: 1) the implementation of a minimized system model whose rank is determined by the number of protected dc lines, in contrast to the conventional approach in [27] that incorporates both dc lines and capacitors; and 2) more critically, the deployment of reduced-order observers in our work whose ranks are substantially smaller than the full-order observers employed in [27], as demonstrated by the theoretical analysis in Section IV-C.

As the proposed method optimizes observer bank design by reducing both the number of observers and their respective ranks, its computational efficiency gets enhanced through the following mechanisms:

1) Reduced matrix operations: Fewer observers mean less observer parameter matrices, which reduces the number of matrix-vector multiplications during real-time signal processing. Lower-order observers further simplify the computations by reducing the size of these matrices, leading to fewer arithmetic operations and faster execution.
2) Lower memory and storage requirements: With fewer lower-order observers, the method requires less memory to store observer parameter matrices and intermediate computational results. This is particularly advantageous for real-time systems with limited computational resources.
3) Reduced data handling overhead: Processing fewer observers and lower-dimensional signals decreases the amount of data that needs to be transferred and manipulated during each computation cycle.

In summary, by employing fewer and lower-order observers, the proposed method achieves a higher computational efficiency.

2) Practicality: The proposed method demonstrates significant advancements in practicality over the existing model-based SAFD approach presented in [27], primarily through its independence from capacitive line ends and the elimination of threshold-based fault isolation requirements. These improvements are substantiated by two key aspects: system configuration adaptivity and fault isolation methodology.

Regarding system configuration adaptivity, while the dc microgrid studied in [27] mandates the installation of shunt capacitors at every network node, the proposed method maintains reliable operation regardless of capacitive element presence. This capability has been experimentally verified through both simulation and experimental tests.

Regarding fault isolation methodology, the determination of threshold for fault isolation involves computationally intensive

TABLE VIII
COMPARISON WITH THE EXISTING MODEL-BASED METHOD [27]

Item	Existing model-based method [27]	The proposed method
minimum No. of observers	= No. of protected lines	= $\lceil \log_2 (\text{No. of protected lines} + 1) \rceil$
Order of observer	= No. of protected lines + No. of nodes	< No. of protected lines
reliance on shunt capacitor	Yes	No
threshold setting for fault isolation	Yes	No

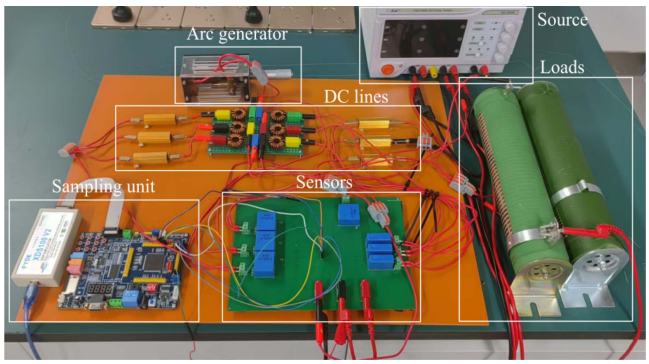

Fig. 14. Photo of hardware setup.

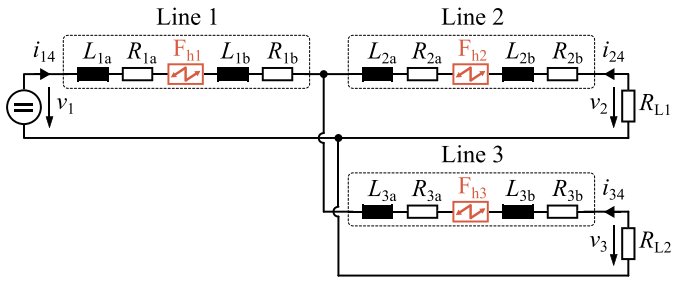

Fig. 15. Circuit diagram of hardware setup.

inequality calculations and is highly sensitive to system parameters, making the method in [27] complicated to implement in real-world scenarios. In contrast, the proposed method introduces a "settingless" fault signature recognition mechanism, which identifies faulty lines through reconstruction error calculation. This approach eliminates the need for complex threshold determination, thereby significantly improving the feasibility of practical implementation.

In summary, the proposed method offers a more practical solution compared with the existing SAFD approach, as evidenced by its adaptivity in system configuration and its setting fault isolation mechanism.

Table VIII presents a comprehensive comparison of the two model-based methods across multiple dimensions.

VI. EXPERIMENTAL VERIFICATION

To understand the performance of the proposed method in a realistic condition, experimental tests were carried out on laboratory hardware.

A. Test Setup

Fig. 14 demonstrates the hardware of the experimental test setup, whose circuit diagram is depicted in Fig. 15. The parameters of the system are listed in Table IX. The experimental dc grid is a four-terminal system configured in a star topology. It consists of a constant dc voltage source and two resistive loads, interconnected through three dc lines. Each line is modeled using two sets of series-connected RL components. At the midpoint of each line, an arc generator can be connected in series.

In signal acquisition, we utilize LV 25-P voltage sensors to measure node voltages and LAH 25-NP current sensors to measure line currents. The acquired signals undergo analog-to-digital conversion via a digital signal processor (DSP) board embedded with TMS320F28335 chip, where analog signals are digitized at a 100 kHz sampling rate. This digital data stored in the DSP is further exported as. dat files.

For signal processing, MATLAB is employed to read the. dat files, transforming the data from hexadecimal to single-precision floating-point format. The measurement data, initially in the range of 0–3 V, is subsequently rescaled to reflect the original voltage and current values.

TABLE IX
PARAMETERS OF EXPERIMENTAL SETUP

Component	Value
source voltage v_{in}	30 V DC
line resistance R_{ia}, R_{ib} $(i = 1, 2, 3)$	0.1 Ω
line inductance L_{ia}, L_{ib} $(i = 1, 2, 3)$	47 μH
load resistance R_{L1}	10 Ω
load resistance R_{L2}	23.4 Ω

TABLE X
SENSITIVITY MATRIX

	F_{h1}	F_{h2}	F_{h3}
Observer 1	1	1	0
Observer 2	1	0	1

B. Test Design

Under each test, the arc generator is connected in series into one of the dc lines, emulating an SAF. To detect and recognize the three different SAFs, a bank of two observers were built in the design process explained in Section IV. The sensitivity of the observer bank is presented in Table X. With the voltage and current data measured from the laboratory dc microgrid,

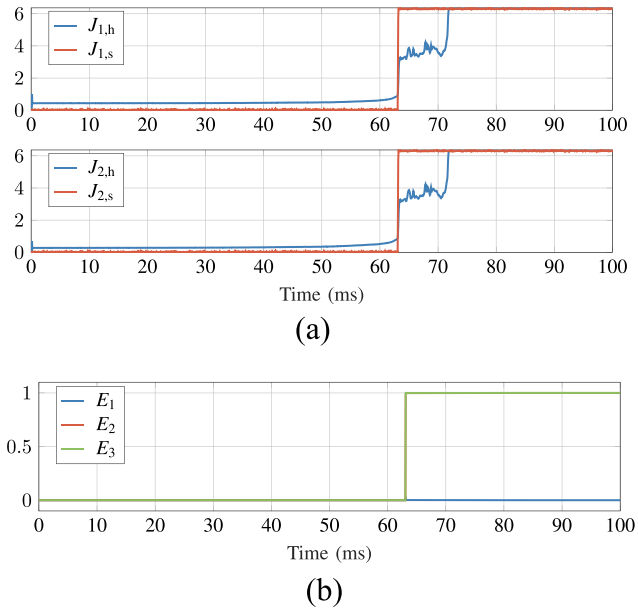

Fig. 16. (a) Residual norms and (b) Reconstruction errors during the SAF F_{h1} in the hardware test.

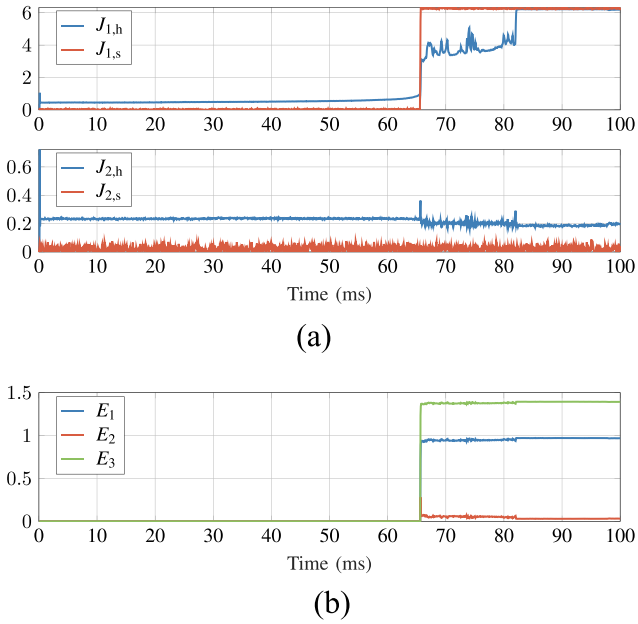

Fig. 17. (a) Residual norms and (b) Reconstruction errors during the SAF F_{h2} in the hardware test.

the residual norms as well as the reconstruction errors were obtained from the observer bank in MATLAB. For comparison, the residual norms derived with simulation data under the same scenarios are also included.

C. Test Results

Figs. 16–18 show the residual norms and reconstruction errors under the three fault scenarios. As seen in Figs. 16(a) to 18(a), the hardware-based residual norms ($J_{m,\mathrm{h}}$, $m = 1, 2$, blue

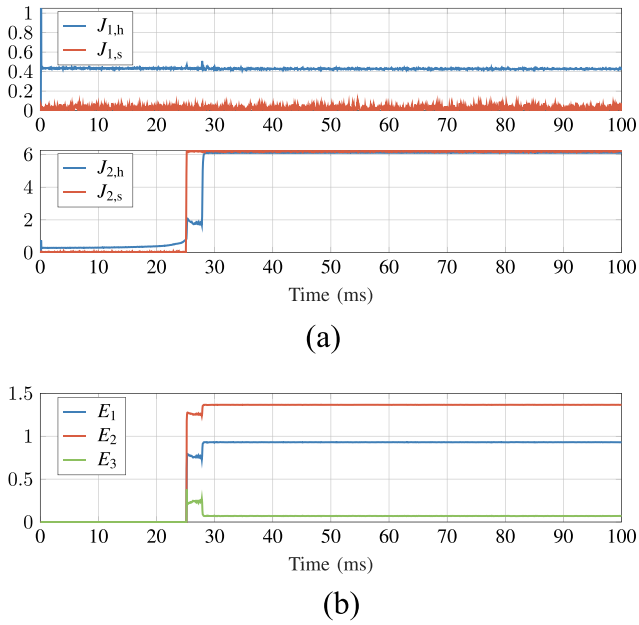

Fig. 18. (a) Residual norms and (b) Reconstruction errors during the SAF F_{h3} in the hardware test.

curves) and simulation-based residual norms ($J_{m,\mathrm{s}}$, $m = 1, 2$, red curves) exhibit nearly identical temporal patterns during various SAFD events and converge to the same steady-state values: Under SAF F_{h1}, both observers generate high residuals after fault; Under SAF F_{h2}, only Observer 1 generates a high residual; Under SAF F_{h3}, only Observer 2 generates a high residual. This close agreement demonstrates the method's consistency across both experimental and simulated conditions.

Notably, $J_{m,\mathrm{h}}$ is slightly higher than $J_{m,\mathrm{s}}$ under pre-fault normal operating conditions. The difference arises because $J_{m,\mathrm{h}}$ incorporates parametric and measurement uncertainties inherent to the hardware setup, whereas $J_{m,\mathrm{s}}$ is derived from idealized numerical simulations that exclude such uncertainties. Besides, $J_{m,\mathrm{h}}$ exhibits a transient response lasting several milliseconds before reaching steady-state, unlike $J_{m,\mathrm{s}}$ which change in a stepwise manner. This is attributed to the fact that the SAFDs in the hardware tests were generated by manually separating the electrodes in the arc generator, whereas the simulation models them as abrupt changes in line resistances.

These minor differences in experimental conditions do not affect the method's fault diagnostic decisions. As clearly shown in Figs. 16(b)–18(b), the reconstruction error (E_h, $h = 1, 2, 3$) for each fault in the hardware test consistently maintains a significantly lower magnitude compared with the reconstruction errors of other faults. This substantial error margin provides strong fault discriminability and robustness of the proposed method in the presence of implementation variations.

VII. Conclusion

This article introduces a novel model-based SAFD method for dc microgrids, which is a centralized scheme for simultaneously detecting SAFs occurring in different segments. The proposed

method brings several improvements. First, the proposed method has good applicability to multiterminal dc microgrids without requiring auxiliary hardware, special sensors and prior fault data. Second, the proposed method has a reduced computational complexity. Third, the pattern recognition-based fault isolation scheme simplifies the implementation and enhances the robustness of the proposed method. In the verification tests, the proposed method demonstrates excellent performance, detecting and isolating various SAFs in a multiterminal dc microgrid with a short sampling delay of 10 ms. Moreover, the proposed method is proven to be robust against abrupt load disturbances, severe modeling errors up to 900% of nominal values, and heavy measurement noises up to 30 dB. Overall, the proposed method offers a promising solution to SAFD in multiterminal dc microgrids.

REFERENCES

[1] T. Dragičević, X. Lu, J. C. Vasquez, and J. M. Guerrero, "DC microgrids—Part I: A review of control strategies and stabilization techniques," *IEEE Trans. Power Electron.*, vol. 31, no. 7, pp. 4876–4891, Jul. 2016.

[2] E. Tisserand, J. Lezama, P. Schweitzer, and Y. Berviller, "Series arcing detection by algebraic derivative of the current," *Electric Power Syst. Res.*, vol. 119, pp. 91–99, 2015.

[3] Q. Lu, Z. Ye, M. Su, Y. Li, Y. Sun, and H. Huang, "A DC series arc fault detection method using line current and supply voltage," *IEEE Access*, vol. 8, pp. 10134–10146, 2020.

[4] A. Shekhar, L. Ramírez-Elizondo, S. Bandyopadhyay, L. Mackay, and P. Bauera, "Detection of series arcs using load side voltage drop for protection of low voltage DC systems," *IEEE Trans. Smart Grid*, vol. 9, no. 6, pp. 6288–6297, Nov. 2018.

[5] Y. Abdullah et al., "Hurst-exponent-based detection of high-impedance DC arc events for 48-V systems in vehicles," *IEEE Trans. Power Electron.*, vol. 36, no. 4, pp. 3803–3813, Apr. 2021.

[6] N. L. Georgijevic, M. V. Jankovic, S. Srdic, and Z. Radakovic, "The detection of series arc fault in photovoltaic systems based on the arc current entropy," *IEEE Trans. Power Electron.*, vol. 31, no. 8, pp. 5917–5930, Aug. 2016.

[7] H.-P. Park and S. Chae, "DC series arc fault detection algorithm for distributed energy resources using arc fault impedance modeling," *IEEE Access*, vol. 8, pp. 179039–179046, 2020.

[8] J.-C. Gu, D.-S. Lai, J.-M. Wang, J.-J. Huang, and M.-T. Yang, "Design of a DC series arc fault detector for photovoltaic system protection," *IEEE Trans. Ind. Appl.*, vol. 55, no. 3, pp. 2464–2471, May/Jun. 2019.

[9] S. Chen, X. Li, and J. Xiong, "Series arc fault identification for photovoltaic system based on time-domain and time-frequency-domain analysis," *IEEE J. Photovolt.*, vol. 7, no. 4, pp. 1105–1114, Jul. 2017.

[10] X. Yao, L. Herrera, S. Ji, K. Zou, and J. Wang, "Characteristic study and time-domain discrete- wavelet-transform based hybrid detection of series DC arc faults," *IEEE Trans. Power Electron.*, vol. 29, no. 6, pp. 3103–3115, Jun. 2014.

[11] Q. Xiong et al., "Series arc fault detection and localization in DC distribution system," *IEEE Trans. Instrum. Meas.*, vol. 69, no. 1, pp. 122–134, Jan. 2020.

[12] H.-P. Park, S.-J. Chang, J.-Y. Park, M. Kim, W. Kim, and S. Chae, "DC series arc fault detection method with resonant filter design for PV systems," *IEEE Trans. Power Electron.*, vol. 39, no. 11, pp. 14240–14250, Nov. 2024.

[13] W. Miao, Z. Wang, F. Wang, K. H. Lam, and P. W. T. Pong, "Multicharacteristics arc model and autocorrelation-algorithm based arc fault detector for DC microgrid," *IEEE Trans. Ind. Electron.*, vol. 70, no. 5, pp. 4875–4886, May 2023.

[14] S. Zhao, Y. Wang, F. Niu, C. Zhu, Y. Xu, and K. Li, "A series DC arc fault detection method based on steady pattern of high-frequency electromagnetic radiation," *IEEE Plasma Sci.*, vol. 47, no. 9, pp. 4370–4377, Sep. 2019.

[15] R. D. Telford, S. Galloway, B. Stephen, and I. Elders, "Diagnosis of series DC arc faults—A machine learning approach," *IEEE Trans. Ind. Informat.*, vol. 13, no. 4, pp. 1598–1609, Aug. 2017.

[16] V. Le, X. Yao, C. Miller, and B.-H. Tsao, "Series DC arc fault detection based on ensemble machine learning," *IEEE Trans. Power Electron.*, vol. 35, no. 8, pp. 7826–7839, Aug. 2020.

[17] P. Dash, S. Rekha Pattnaik, E. N. V. D. V. Prasad, and R. Bisoi, "Detection and classification of DC and feeder faults in DC microgrid using new morphological operators with multi class AdaBoost algorithm," *Appl. Energy*, vol. 340, 2023, Art. no. 121013.

[18] Z. Gao, C. Cecati, and S. X. Ding, "A survey of fault diagnosis and fault-tolerant techniques–Part I: Fault diagnosis with model-based and signal-based approaches," *IEEE Trans. Ind. Electron.*, vol. 62, no. 6, pp. 3757–3767, Jun. 2015.

[19] S. Zhuo, A. Gaillard, L. Xu, C. Liu, D. Paire, and F. Gao, "An observer-based switch open-circuit fault diagnosis of DC-DC converter for fuel cell application," *IEEE Trans. Ind. Appl.*, vol. 56, no. 3, pp. 3159–3167, May/Jun. 2020.

[20] X. Ding, J. Poon, I. Čelanović, and A. D. Domínguez-García, "Fault detection and isolation filters for three-phase AC-DC power electronics systems," *IEEE Trans. Circuits Syst. I: Reg. Papers*, vol. 60, no. 4, pp. 1038–1051, Apr. 2013.

[21] S. Shao, P. W. Wheeler, J. C. Clare, and A. J. Watson, "Fault detection for modular multilevel converters based on sliding mode observer," *IEEE Trans. Power Electron.*, vol. 28, no. 11, pp. 4867–4872, Nov. 2013.

[22] T. Wang et al., "Model-based fault detection and isolation in DC microgrids using optimal observers," *IEEE Trans. Emerg. Sel. Topics Power Electron.*, vol. 9, no. 5, pp. 5613–5630, Oct. 2021.

[23] T. Wang, L. Liang, Z. Hao, A. Monti, and F. Ponci, "LPV model-based fault detection and isolation in DC microgrids through signature recognition," *IEEE Trans. Smart Grid*, vol. 14, no. 4, pp. 2558–2571, Jul. 2023.

[24] S. Tan, P. Xie, J. M. Guerrero, J. C. Vasquez, and R. Han, "Cyberattack detection for converter-based distributed DC microgrids: Observer-based approaches," *IEEE Ind. Electron. Mag.*, vol. 16, no. 3, pp. 67–77, Sep. 2022.

[25] A. J. Gallo, M. S. Turan, F. Boem, T. Parisini, and G. Ferrari-Trecate, "A distributed cyber-attack detection scheme with application to DC microgrids," *IEEE Trans. Autom. Control*, vol. 65, no. 9, pp. 3800–3815, Sep. 2020.

[26] W. Miao, F. Zhi, F. Wang, X. Zhou, and Y. Luo, "Arc fault detection and location technique based on state space modeling for DC microgrid," in *Proc. 7th Int. Conf. Power Renewable Energy*, 2022, pp. 452–457.

[27] X. Yao, V. Le, and I. Lee, "Unknown input observer-based series DC arc fault detection in DC microgrids," *IEEE Trans. Power Electron.*, vol. 37, no. 4, pp. 4708–4718, Apr. 2022.

[28] G. Yang, L. K. Marepalli, L. Herrera, and X. Yao, "Series DC arc fault detection in DC microgrids based on distributed unknown input observers," *IEEE Trans. Transport. Electrific.*, vol. 10, no. 3, pp. 4766–4781, Sep. 2024.

[29] J. Chen and R. J. Patton, *Robust Model-Based Fault Diagnosis for Dynamic Systems*. New York, Ny, USA: Springer Science & Business Media, 1999.

[30] J. Chen, R. J. Patton, and H.-Y. Zhang, "Design of unknown input observers and robust fault detection filters," *Int. J. Control*, vol. 63, no. 1, pp. 85–105, 1996.

[31] M. Hou and P. C. Muller, "Design of observers for linear systems with unknown inputs," *IEEE Trans. Autom. Control*, vol. 37, no. 6, pp. 871–875, Jun. 1992.

[32] S. Guo, F. Zhu, and B. Jiang, "Reduced-order switched UIO design for switched discrete-time descriptor systems," *Nonlinear Anal.: Hybrid Syst.*, vol. 30, pp. 240–255, 2018.

[33] T. Wang, L. Liang, Z. Hao, A. Monti, and F. Ponci, "A comprehensive fault detection and isolation method for DC microgrids using reduced-order unknown input observers," *IEEE Trans. Power Del.*, vol. 39, no. 1, pp. 479–495, Feb. 2024.

[34] R. F. Ammerman, T. Gammon, P. K. Sen, and J. P. Nelson, "DC-arc models and incident-energy calculations," *IEEE Trans. Ind. Appl.*, vol. 46, no. 5, pp. 1810–1819, Sep./Oct. 2010.

[35] O. A. Sotomayor and D. Odloak, "Observer-based fault diagnosis in chemical plants," *Chem. Eng. J.*, vol. 112, no. 1-3, pp. 93–108, 2005.

[36] M. Hou and P. C. Müller, "Fault detection and isolation observers," *Int. J. Control*, vol. 60, no. 5, pp. 827–846, 1994.

[37] S. Lu, B. Phung, and D. Zhang, "A comprehensive review on DC arc faults and their diagnosis methods in photovoltaic systems," *Renewable Sustain. Energy Rev.*, vol. 89, pp. 88–98, 2018.

[38] K. M. Armijo, J. Johnson, M. Hibbs, and A. Fresquez, "Characterizing fire danger from low-power photovoltaic arc-faults," in *Proc. IEEE 40th Photovoltaic Specialist Conf.*, 2014, pp. 3384–3390.

Ting Wang (Member, IEEE) received the B.E. degree in electrical engineering and automation from Xi'an Jiaotong University, Xi'an, China, in 2009, and the M.Sc. degree in electrical power engineering and the Ph.D. degree in electrical engineering from RWTH Aachen University, Aachen, Germany, in 2012 and 2021, respectively.

From 2012 to 2017, he worked with ABB in different departments in Beijing and Xi'an, China. From 2017 to 2021, He was a Research Associate with the Institute for Automation of Complex Power Systems, E.ON Energy Research Center, RWTH Aachen University, Aachen, Germany. From 2022 to 2024, he was a Research Fellow with the School of Electrical and Electronic Engineering, Nanyang Technological University, Singapore. Since 2024, he has been an Associate Professor with the school of Electrical Engineering, Xi'an Jiaotong University, Xi'an, China. His research interests include protection and control of dc microgrids.

Yanxin Chen received the bachelor's degree in electrical engineering and automation from Sichuan University, Chengdu, China, in 2023. He is currently working toward the M.Sc. degree in electrical engineering with Xi'an Jiaotong University, Xi'an, China.

His research focuses on the protection of dc collection grids in offshore wind farms.

Wei Liu received the bachelor's and M.Sc. degrees in electrical engineering from Xi'an Jiaotong University, Xi'an, China, in 2022 and 2025, respectively.

He is current working with NARI Technology Company, Ltd., Nanjing, China. His research focuses on the protection of dc microgrids.

Zhiguo Hao (Senior Member, IEEE) received the bachelor's and Ph.D. degrees in electrical engineering from Xi'an Jiaotong University, Xi'an, China, in 1998 and 2006, respectively.

From 2015 to 2016, He was a Visiting Scholar with The Ohio State University, Columbus, OH, USA. He is currently a Professor and the Associate Dean with the School of Electrical Engineering, Xi'an Jiaotong University. His research interests include multiparameter protection and safe operation of power transformers, relay protection principles and technologies for ac/dc power grids, protection and control of power systems with renewable energy sources.

Antonello Monti (Senior Member, IEEE) received the M.Sc degree (*summa cum laude*) and the Ph.D. degree in electrical engineering from Politecnico di Milano, Milano, Italy, in 1989 and 1994, respectively.

He started his career in Ansaldo Industria and then moved in 1995 to Politecnico di Milano as Assistant Professor. In 2000, he joined the Department of Electrical Engineering, University of South Carolina (USA) as an Associate and then Full Professor. Since 2008, he has been the Director of the Institute for Automation of Complex Power System within the E.ON Energy Research Center, RWTH Aachen University. Since 2019, he holds a double appointment with Fraunhofer FIT where he is developing the new Center for Digital Energy, Aachen, Germany. Currently, his is leading ERC Synergy Project SAFEr Grid (Store-and-Forward Energy Grid).

Dr. Monti is author or co-author of more than 400 peer-reviewed papers published in international Journals and in the proceedings of International conferences. He is an Associate Editor of the *IEEE System Journal*, an Associate Editor of *IEEE Electrification Magazine*, Member of the Editorial Board of the Elsevier Journal *SEGAN* and Member of the founding board of the Springer Journal *Energy Informatics*. He was the recipient of the 2017 IEEE Innovation in Societal Infrastructure Award.

Ferdinanda Ponci (Senior Member, IEEE) received the Ph.D. degree in electrical engineering from the Politecnico di Milano, Milano, Italy, in 2002.

She joined the Department of Electrical Engineering, University of South Carolina, Columbia, SC, USA, as an Assistant Professor, in 2003 and was tenured and promoted in 2008. In 2009, she joined the Institute for Automation of Complex Power Systems, E.ON Energy Research Center, RWTH Aachen University, Aachen, Germany, where she is currently a Professor for Monitoring and Distributed Control for Power Systems. Her research interests include advanced measurement, monitoring and automation of active distribution systems.

Dr. Ponci is a member of the Administration Committee of the IEEE Instrumentation and Measurement Society and the Liaison with IEEE Women in Engineering.